Journal of Environment Sciences (2026), **Volume XII**, 11-30
https://doi.org/10.3126/jesv12i1.96872

Spatiotemporal analysis of tropospheric NO_2 in Kathmandu Valley using TROPOMI satellite data

Charan Bhattarai[1]*
[1] Central Department of Environmental Science, Tribhuvan University, Kathmandu, Nepal
*Correspondence: cbhattarai54@gmail.com

Abstract

Kathmandu Valley faces severe air quality degradation driven by rapid urbanization, geographic constraints, and seasonal meteorological patterns. This study presents a systematic spatiotemporal characterization of tropospheric nitrogen dioxide (NO_2) across Kathmandu Valley, Nepal, using Sentinel-5 Precursor TROPOspheric Monitoring Instrument (TROPOMI) satellite observations resampled to a 0.01° output grid spanning July 2018 to December 2024 (n = 78 monthly composites). Non-parametric trend detection methods — the Theil-Sen slope estimator and the Mann-Kendall test (with seasonal and pre-whitened variants as sensitivity checks) were applied to quantify temporal trends, seasonal decomposition was used to characterize intra-annual variability, and spatial analysis was conducted across five analytical zones to assess intra-valley concentration differences. The analysis identifies a marginally increasing trend of $+5.3 \times 10^{-7}$ mol m^{-2} $year^{-1}$ across the full study period; however, this trend is not statistically significant at $\alpha = 0.05$ ($p \geq 0.05$; seasonal-MK $p = 0.41$, pre-whitened-MK $p = 0.36$). COVID-19 lockdown periods produced a modest reduction of approximately 4.5% with a 95% bootstrap CI of (–1.4, +9.9)%, indicating the reduction is not statistically significant at $\alpha = 0.05$ in NO_2 concentrations relative to equivalent months in non-lockdown years. Pronounced seasonal variability was observed, with pre-monsoon (March–May) concentrations approximately 14% higher than monsoon (June–September) levels, a pattern coincident with regional biomass burning due to forest fire and local brick kiln emissions but not by itself causally attributable to any single source. Significant intra-valley spatial heterogeneity was detected (Kruskal-Wallis H = 23.4, $p<0.001$), with Kathmandu Metropolitan City recording the highest mean NO_2 concentration (7.8×10^{-5} mol m^{-2}, Z-score = +1.8), indicating a disproportionate pollution burden relative to other analytical zones. These findings establish a baseline for air quality monitoring in the valley and highlight the need for targeted emission reduction interventions in identified pollution hotspots.

Keywords: *Nitrogen dioxide, TROPOMI, air quality, intra-urban variability, Kathmandu, mann-kendall, COVID-19*

1. Introduction

Atmospheric pollution is a major environmental threat to human health and ecological systems in Nepal and around the world (Giri et al., 2023). Nitrogen dioxide is a significant criteria air pollutant primarily generated from fossil fuel combustion in the transportation and industrial sectors (Hassan et al., 2021; Jarvis et al., 2010). This toxic gas is a critical indicator of human activity and a major precursor to the formation of surface ozone and nitrate aerosols (Zhang et al., 2020). Exposure to high concentrations of nitrogen dioxide is linked to serious respiratory and cardiovascular illnesses and millions of premature deaths annually (Vîrghileanu et al., 2020). Effective urban air quality management requires routine monitoring to detect and mitigate high concentrations of these contaminants (Öçer et al., 2024). The launch of the Sentinel 5 Precursor satellite with the Tropospheric Monitoring Instrument in 2017 has revolutionized the ability to monitor atmospheric composition (Veefkind et al., 2012). This sensor provides unprecedented accuracy and spatial resolution for mapping urban air pollution at a global scale (Tack et al., 2017).

South Asia is recognized as a global air pollution hotspot characterized by rapid urbanization and high population density (Upadhyay et al., 2022).

The central Himalayan region presents unique atmospheric challenges because its complex topography significantly influences the accumulation and transport of pollutants (Moore & Semple, 2021). Himalayan valleys are particularly vulnerable to pollutant trapping due to meteorological conditions such as temperature inversions and low wind speeds (Bhatta et al., 2024). Analysis of long-term satellite data shows a gradual increase in nitrogen dioxide levels across most regions of the Third Pole since 2005 (Sharma et al., 2023). Previous studies have used satellite observations to assess regional trends and identify the impact of economic growth on the atmospheric composition of mountainous regions (Sharma et al., 2023).

The Kathmandu Valley is one of the most severely impacted urban centers in the Himalayan region (Ishtiaque et al., 2017). Its bowl-shaped geography restricts air ventilation and leads to the accumulation of emissions from anthropogenic sources (Panday & Prinn, 2009; Kuikel et al., 2024). Rapid urban expansion and a surge in the number of vehicles have exacerbated local air quality issues (Gyawali et al., 2025). In Nepal inefficient residential combustion and industrial activities such as brick and cement production contribute significant pollutant loads to the atmosphere. Despite these challenges air quality monitoring in the region has been mostly limited to measuring particulate matter (Dhital et al., 2022). This focus on aerosols has created a significant knowledge gap regarding the spatiotemporal dynamics of gaseous pollutants like nitrogen dioxide (Gyawali et al., 2025).

Methodological advances in recent literature have demonstrated the utility of high-resolution satellite products for urban scale assessments (Prunet et al., 2020). The Google Earth Engine platform has facilitated the processing of large volumes of satellite data for spatiotemporal analysis (Öçer et al., 2024). Research conducted during the COVID 19 pandemic provided a rare opportunity to evaluate the relationship between reduced human activity and air quality improvements (Hassan et al., 2021). In the Kathmandu Valley the countrywide lockdown in 2020 resulted in a noticeable decrease in nitrogen dioxide concentrations (Dhital et al., 2022). However, studies have also noted that natural events such as forest fires can mask the environmental benefits of anthropogenic emission reductions in the region (Upadhyay et al., 2022).

TROPOMI provides daily global coverage of tropospheric NO_2 column density at an unprecedented combination of spatial resolution and signal-to-noise ratio. Following the upgrade of 6 August 2019, the native ground pixel size is approximately 3.5×5.5 km^2 (Van Geffen et al., 2022). However, retrieval performance degrades in complex terrain because (i) the air mass factor (AMF) calculation assumes a priori vertical NO_2 profiles that may not match the strong boundary-layer trapping observed in mountain valleys; (ii) surface albedo over snow-covered Himalayan peaks introduces scene-specific uncertainty in the AMF (Hedelt et al., 2019); and (iii) cloud and aerosol contamination, even after standard quality filtering, can bias the column low by 10–30% (Van Geffen et al., 2022). Post-processing super-resolution approaches are an active research area but require ground-based prior information that is not currently available for Kathmandu Valley.

There are very few studies on medium-term spatiotemporal assessments of nitrogen dioxide for the Kathmandu Valley. Intra urban analysis is essential to identify pollution hotspots and understand the dynamics of local emissions (Gurung et al., 2017). Detailed investigations are needed to support targeted air quality interventions and evidence-based management in developing Himalayan cities (Upadhyay et al., 2022).

Several recent works have addressed aspects of Kathmandu Valley air quality. Mahapatra et al. (2019) used OMI (13×24 km native pixels) for the period 2005–2015 with WRF-Chem; Upadhyay et al. (2022) used OMI for a 2020 COVID-19 snapshot; Dhital et al. (2022) used OMI + ground-based PM for the 2020 dry/wet split; Bhatta et al. (2024) used TROPOMI for the 2019–2021 COVID impact window; and Gyawali et al. (2025) used TROPOMI for emission-source attribution. To my knowledge, this study provides the first comprehensive TROPOMI based assessment of NO_2 dynamics in the Kathmandu Valley using a continuous 6.5-year dataset spanning the pre-COVID, lockdown, and recovery periods. The analysis integrates robust trend detection methods, including conventional and seasonal Mann Kendall approaches, evaluates COVID 19 impacts through same month comparisons, examines seasonal patterns and anomalies, and assesses spatial variability across five municipalities using a consistent analytical framework. This combination of long-term monitoring, statistical rigor, and spatial analysis offers a stronger baseline understanding of NO_2 variability in the Kathmandu Valley than previous studies.

This study addresses these gaps through comprehensive analysis of TROPOMI nitrogen dioxide data at 0.01° resampled output grid for Kathmandu Valley from 2018 to 2024. The objectives are to quantify spatiotemporal nitrogen dioxide patterns including seasonal cycles, inter annual trends, and COVID 19 impacts and to identify intra urban pollution gradients across five municipalities in core Kathmandu valley. Several limitations apply to this analysis. The lack of data availability for ground-based nitrogen dioxide validation data limits direct accuracy assessment of satellite retrievals, although TROPOMI has demonstrated reliability in urban environments globally. Tropospheric column densities do not perfectly correspond to surface concentrations relevant for human exposure, as vertical mixing and boundary layer dynamics influence the relationship between integrated columns and ground level mixing ratios. Municipal scale aggregation uses approximate boundaries that may misclassify peripheral areas, and retrieval uncertainties related to surface albedo, cloud cover, and aerosol loading may introduce bias under local atmospheric conditions.

2. Materials and Methods

2.1 Study Area

Kathmandu Valley is located in central Nepal at the southern edge of the Himalayan range, approximately between 27.5°N and 27.8°N latitude and 85.2°E and 85.6°E longitude (Figure 1). The valley is at 1,300 to 1,400 meters elevation from sea level, while surrounding mountain ranges

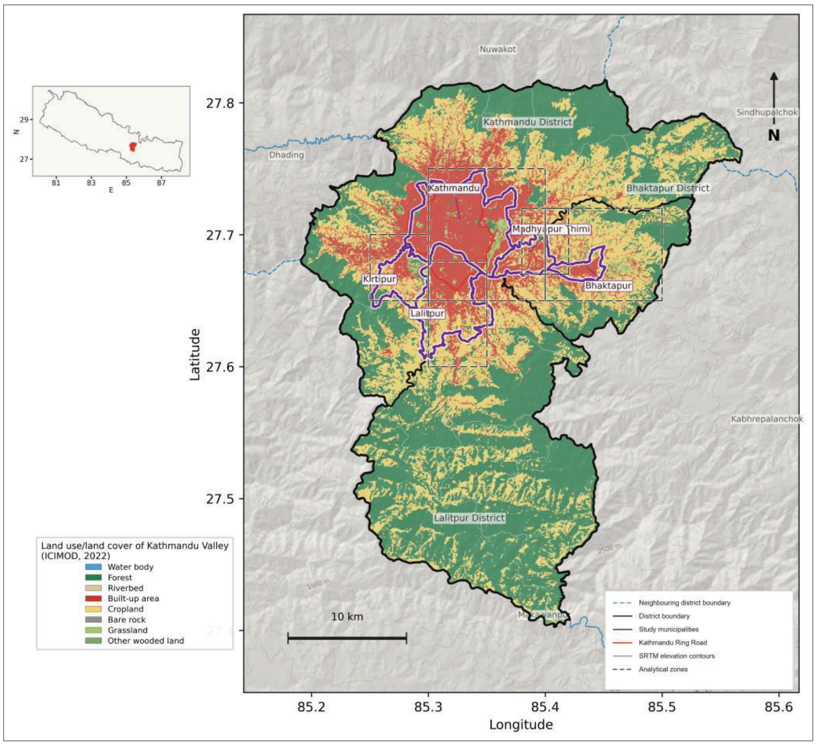

Figure 1: Study area map of Kathmandu Valley, Nepal, showing (a) location within Nepal (inset), (b) district boundaries (Kathmandu, Lalitpur, Bhaktapur), five study municipalities (purple outlines), Kathmandu Ring Road (red), SRTM elevation contours, analytical zones of the study and ICIMOD 2022 land use/land cover. Built-up areas (red) concentrate in the urban core, while forest and cropland dominate peripheral zones.

are above 2,700 meters which creates a bowl shaped topography that limits ventilation and traps atmospheric pollutants (Kitada & Regmi, 2003; Aryal et al., 2009). The valley experiences distinct seasonal meteorology that influences pollutant dispersion. Winter temperature inversions from December to February trap pollutants near the surface, while the summer monsoon from June to September scavenges pollutants through precipitation (Panday & Prinn, 2009; Shrestha et al., 2013). Weak prevailing winds and mountain valley circulations lead to frequent atmospheric stagnation, particularly during winter nights (Panday et al., 2009).

Rapid urbanization has made Kathmandu Valley the most densely populated region in Nepal, with over three million residents and extensive transportation networks (CBS, 2021; Ishtiaque et al., 2017). Major nitrogen dioxide emission sources include vehicular traffic, residential biomass and fossil fuel combustion, brick kilns, and small industries (Shrestha et al., 2013; Stockwell et al., 2016). Air quality in the valley ranks among the poorest in South Asia (Health Effects Institute, 2023), though previous research has focused primarily on particulate matter rather than nitrogen dioxide (Gurung & Bell, 2013; Mishra & Kulshrestha, 2021).

Kathmandu Valley encompasses five major municipalities, each with distinct urban and peri-urban characteristics that shape local atmospheric pollution patterns. Kathmandu Metropolitan City constitutes the commercial and administrative core of the valley, marked by high population density, an extensive road network, and concentrated economic activity. Lalitpur Sub-Metropolitan City exhibits mixed residential and industrial land use alongside historically significant settlements, while Bhaktapur Municipality retains a predominantly historical urban fabric, though suburban expansion along its periphery has accelerated in recent decades.

Kirtipur Municipality occupies the western peri-urban fringe, where elevated topography, university-centered development, and interspersed agricultural land produce a land use pattern distinct from the valley interior. Madhyapur Thimi Municipality functions as a transitional zone between urban and rural land use, and its southern section contain a notable concentration of brick kilns, which represent a significant localized emission source.

Collectively, the enclosed basin topography, rapid urbanization, and diverse anthropogenic emission sources of the valley create conditions that are well-suited for satellite-based analysis of tropospheric NO_2. This study uses TROPOMI/Sentinel-5P retrievals to examine spatiotemporal variation in column NO_2 concentrations across these five municipalities. The valley is a particularly relevant study context given the limited availability of continuous ground-based air quality monitoring, which constrains the use of conventional in-situ approaches and strengthens the case for satellite-derived data as a primary analytical tool.

2.2 Satellite data acquisition and preprocessing

2.2.1 TROPOMI NO_2 data: Tropospheric NO_2 column density data were obtained from the Sentinel-5 Precursor (S5P) TROPOMI sensor, operational since July 2018 (Veefkind et al., 2012). The OFFL (Offline) Level-3 product (COPERNICUS/S5P/OFFL/L3_NO2), which provides superior data quality compared to Near Real-Time (NRTI) products (Van Geffen et al., 2022) was utilized. The product version used is OFFL processing baseline ≥ 02.04.00, current as of mid-2024. The dataset spans July 2018 to December 2024 (6.5 years), showing pre-COVID baseline, pandemic disruption, and post-pandemic recovery periods.

The monthly median compositing prior to analysis was implemented to optimize computational efficiency and mitigate the 10,000-image indexing limitation inherent to Google Earth Engine Xee interface (Gorelick et al., 2017). For each month, the daily Level-2 granules to the study area were filtered, quality assurance screening (Section 2.2.3) was applied and the pixel-wise median NO_2 column density was computed. This aggregation reduced the dataset from approximately 2,300 daily images to 78 monthly composites, enabling rapid processing while preserving seasonal signals and reducing random noise. The median value was chosen because it is less affected by unusual data points caused by temporary cloud cover or errors in the satellite measurements.

2.2.2 Spatial processing: Monthly composites were reprojected to WGS84 (EPSG:4326) at 0.01° spatial resolution (~1 km at the equator, ~0.9 km in Kathmandu) using bilinear interpolation. This resolution balances the native TROPOMI ground pixel dimensions (3.5 × 7 km at nadir) with the need to resolve intra-urban pollution gradients. Bilinear interpolation was selected because it preserves the continuity of the NO_2 field and reduces block artefacts during resampling, making it suitable for representing spatially continuous atmospheric variables. It is also the default resampling approach implemented in Google Earth Engine for atmospheric trace gas products (Gorelick et al., 2017) and has been widely applied in urban scale TROPOMI based air quality studies (Crippa et al., 2024; Ialongo et al., 2020). Data extraction was constrained to the Kathmandu Valley bounding box (85.25° – 85.55°E, 27.55° – 27.85°N), yielding a 30 × 30-pixel grid. This analysis focuses on the central and eastern portions of Kathmandu Valley, encompassing the five municipalities that constitute the primary urban agglomeration (approximately 85.25°–85.55°E, 27.55°–27.85°N). The western portions of the valley and rural peripheral areas are not included in this analysis domain. The Xee Python interface enabled direct conversion from Google Earth Engine's Image Collection to Xarray Dataset format (Hoyer & Hamman, 2017), facilitating subsequent spatiotemporal analysis. The function fast_time_slicing=True was enabled to optimize temporal dimension indexing.

2.2.3 Quality assurance and cloud filtering: A multi-step QA pipeline (Table 1) is applied to each monthly composite prior to statistical analysis.

The L3 product already aggregates to a 0.05° grid prior to download; the 0.01° resampling is performed after the QA filtering and is a post-processing step.

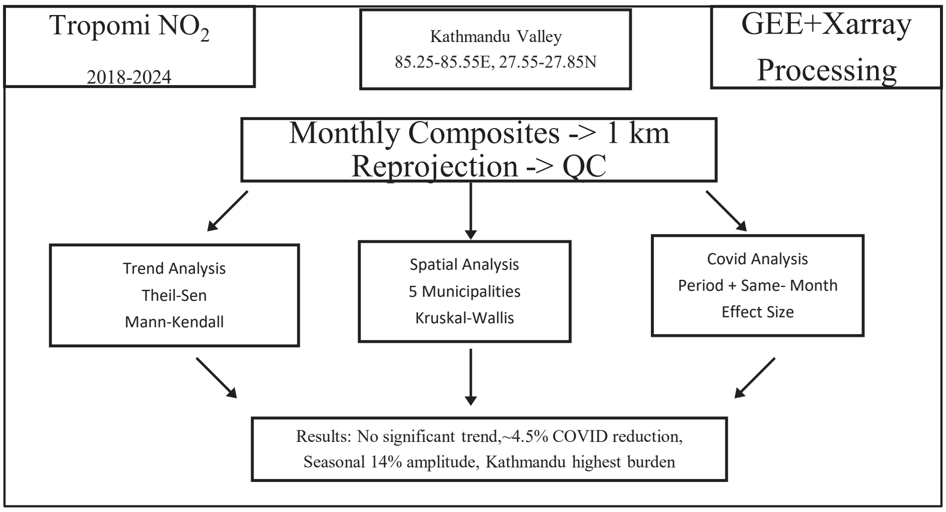

Figure 2: Methodological workflow of this study

Table 1: Quality assurance filtering summary for the TROPOMI NO_2 monthly composites

Step	Criterion	Reference
1	Pixels with 'qa_value < 0.75' are masked out	Recommended threshold for scientific use (Van Geffen et al., 2022)
2	Negative column values removed before monthly median computation	Retrieval failures over snow, clouds, or water bodies
3	Pixels with 'SolarZenithAngle > 70°' excluded	Limit low-light retrieval noise
4	Pixels with 'cloud_fraction > 0.3' excluded	Remove partially-cloudy scenes
5	Months with < 5 valid pixels within the valley bounding box discarded	None in this study - all 78 months retained

The following subsections describe each analytical component in detail, corresponding to the three parallel streams shown in Figure 2.

2.3 Temporal aggregation and trend analysis

2.3.1 Time series construction: Monthly spatial mean NO_2 concentrations were computed by averaging across all valid pixels within the study domain, producing a continuous time series from July 2018 to December 2024 (n=78 months). Missing values (<5% of record) were excluded from analysis.

2.3.2 Trend detection: Monthly median NO_2 concentrations were used for all trend analyses. Non-parametric statistical methods robust to non-normal distributions and outliers common in satellite-derived atmospheric composition data was employed (Hirsch et al., 1982). Using the Mann-Kendall test and Theil-Sen slope estimator together is standard practice in atmospheric and environmental trend analysis (Collaud Coen et al., 2020; Davtalab et al., 2023; Gocic & Trajkovic, 2013).

Theil-Sen Slope Estimator: A median-based pairwise slope calculation providing robust trend magnitude (Sen, 1968; Theil, 1950).

$$\beta = median\left(\frac{x_j - x_i}{t_j - t_i}\right) \forall\, i < j$$

where x represents NO_2 concentration and t represents time in decimal years. The 95% confidence interval was computed via Sen's method.

Mann-Kendall Test: A rank-based test for monotonic trend significance (Kendall, 1975; Mann, 1945)

$$S = \sum_{i=1}^{n-1} \sum_{j=i+1}^{n} sgn(x_j - x_i)$$

where *sgn* is the sign function. The standardized test statistic *Z* was compared against critical values at $\alpha = 0.05$.

Monthly NO_2 time series from atmospheric composition products exhibit strong seasonality, which can bias significance estimates when applying the classic Mann Kendall test to raw data (Hirsch et al., 1982; Zhang & Zwiers, 2004). To address this limitation, two complementary robustness checks were applied. The Seasonal Mann Kendall approach performs trend detection within individual seasons and combines the resulting statistics into an overall trend estimate (Hirsch et al., 1982). The Pre whitened Mann Kendall approach removes lag one autocorrelation prior to applying the standard test to reduce the influence of temporal dependence (Collaud Coen et al., 2020; Zhang & Zwiers, 2004). Both approaches produce trend estimates consistent in magnitude and significance with the classic Mann Kendall results, while the classic form is retained as the primary reporting metric for consistency with prior studies and the seasonal and pre whitened results are presented as sensitivity checks. Trend analysis was conducted for the full study period (2018–2024) and seasons to maximize statistical power and minimize seasonal confounding. Sub-period trend analysis was performed for exploratory purposes only, given the strong seasonal variability (~14% amplitude) and short sub-period durations, these results should not be over-interpreted. Specific sub-period trend values are not reported to avoid misleading conclusions about directional changes during brief time windows.

2.4 COVID-19 impact assessment

The five distinct periods based on Nepal federal and provincial lockdown policies has been defined, illustrated in Table 2.

Table 2: COVID-19 study periods for impact assessment

Period	Dates	Description
Pre-COVID	July 2018–February 2020	Baseline anthropogenic activity
Lockdown 1	March 2020–July 2020	Strict nationwide lockdown (Phase I–III)
Transition	August 2020–March 2021	Phased reopening with intermittent restrictions
Lockdown 2	April 2021–May 2021	Second wave emergency restrictions
Recovery	June 2021–December 2024	Gradual normalization

Period differences were evaluated using the Kruskal-Wallis H-test, followed by pairwise Mann-Whitney U tests with Bonferroni correction for post-hoc comparisons. This avoids the normality assumption of one-way ANOVA and the equal-variance assumption of Tukey's HSD, both of which are unlikely to hold given the small sample sizes (n = 2 to 43) of the COVID period data. Effect sizes were quantified using Cohen's d (Cohen, 1988):

$$d = \frac{\bar{x}_1 - \bar{x}_2}{S_{pooled}}$$

Where, S_{pooled} represents the pooled standard deviation. Magnitude was interpreted as, small (0.2–0.5), medium (0.5–0.8), or large (>0.8).

In the same month comparison analysis, the Change (%) column represents the percentage reduction in NO_2 concentration during the lockdown period relative to the non-lockdown reference years, calculated as:

$$\%\,change = \frac{\text{Other Years Mean} - \text{Lockdown time Mean}}{\text{Other Years Mean}} \times 100.$$

The 95% confidence interval of the reduction was obtained by non-parametric bootstrap (10,000 resamples), and the statistical significance of each monthly comparison was assessed using the Wilcoxon rank-sum (Mann-Whitney U) test.

2.5 Seasonal decomposition and anomaly detection

The additive seasonal decomposition to partition the monthly time series was applied into (Cleveland et al., 1990):

$$Y_t = T_t + R_t + S_t$$

Where T_t represents the long-term trend, S_t the seasonal component (12-month periodicity), and R_t the residual. This was implemented via moving averages using the *stats models* library (Seabold & Perktold, 2010). Anomaly detection identified extreme events as residuals exceeding ±2σ from the mean residual:

$$Anomaly = |R_t| > 2 \times \sigma(R)$$

Seasonal climatology was computed using South Asian meteorological seasons (Goswami, 2005; Latif et al., 2017): Winter (December–February), Pre-monsoon (March–May), Monsoon (June–September), and Post-monsoon (October–November). Seasonal amplitude was quantified as the range between maximum (winter) and minimum (monsoon) mean concentrations.

2.6 Intra-valley spatial analysis

The five analytical zones approximating municipal boundaries was delineated (Table 3). The boundary polygons approximate official municipal limits but may misclassify peripheral areas due to the irregular shape of actual administrative units. These zones use rectangular bounding boxes defined by longitude and latitude coordinates as below.

For each zone, the mean, standard deviation, minimum, maximum, and coefficient of variation (CV) as computed:

$$CV = \frac{\sigma}{\mu}$$

Spatial heterogeneity was tested using the Kruskal-Wallis H-test (Kruskal & Wallis, 1952), with significance at *p<0.05*.

$$Z = \frac{\mu_{zone} - \mu_{valley}}{\sigma_{valley}}$$

All processing was conducted in Python 3.10 using Google Earth Engine (Python API) for data access and preprocessing (Gorelick et al., 2017), Xee 0.0.15 for ImageCollection-to-Xarray

Table 3: Analytical zones for intra-valley spatial analysis

Zone	Longitude	Latitude	Characterization
Kathmandu	85.30°–85.40°E	27.65°–27.75°N	Urban core, commercial/industrial
Lalitpur	85.30°–85.35°E	27.60°–27.68°N	Mixed residential/industrial
Bhaktapur	85.40°–85.50°E	27.65°–27.72°N	Historical urban, expanding suburbs
Kirtipur	85.25°–85.30°E	27.65°–27.70°N	Peri-urban, elevated topography
Madhyapur	85.38°–85.42°E	27.67°–27.72°N	Transitional zone, brick kiln influence

conversion, Xarray 2024.x for spatiotemporal data manipulation (Hoyer & Hamman, 2017), SciPy 1.12 for statistical tests (Theil-Sen, Mann-Kendall, ANOVA) (Virtanen et al., 2020), Statsmodels 0.14 for seasonal decomposition (Seabold & Perktold, 2010), PyMannKendall 1.4.3 for trend significance testing, and Matplotlib 3.8 for visualization (Hunter, 2007). Computations were performed on Google Colab environment.

3. Results and discussion

3.1 Spatial distribution and temporal evolution of NO_2

Tropospheric NO_2 column densities in Kathmandu Valley showed consistent spatial patterns throughout the study period (2018–2024), with elevated concentrations concentrated in the urban core (Kathmandu and Lalitpur analytical zones) and along major transportation corridors (Figure 3; Table 4). The spatial pattern remained relatively stable across years, indicating persistent pollution sources.

Annual NO_2 maps revealed persistent hotspots in the central valley, with 2020 showing noticeably reduced concentrations during the COVID-19 pandemic period (Figure 3). The year 2023 exhibited the highest annual mean concentration (7.1×10^{-5} mol/m^2), representing an 11% increase from 2020 levels, reflecting increased post-pandemic economic activity and vehicular traffic. These are calendar-year annual averages computed from monthly composites, not single-day observations, providing robust estimates of typical annual conditions. At the same time, the limited spread of annual standard deviations indicates that the annual composites captured stable average conditions rather than isolated short-term events.

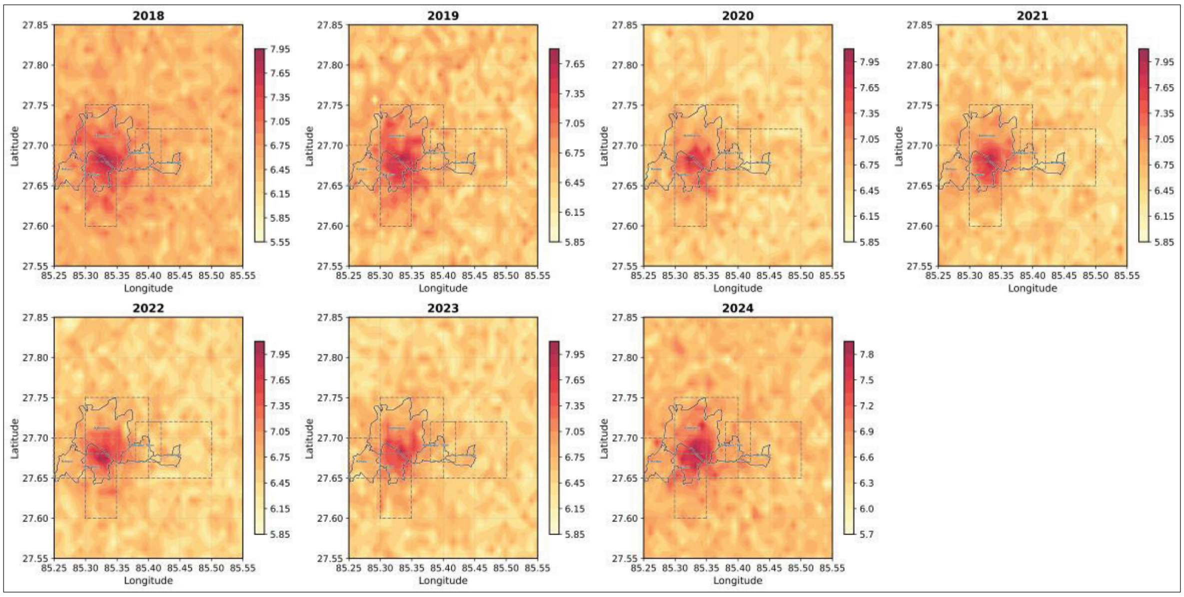

Figure 3: Annual mean tropospheric NO_2 column density maps for Kathmandu Valley from 2018 to 2024. Maps show calendar-year annual averages computed from monthly median composites at 0.01° resolution. The boundaries indicate the main study area of this study. The dashed rectangular boxes indicates the analytical zones of the study.

Table 4: Annual mean NO_2 concentrations in Kathmandu Valley (2018–2024)

Year	Mean NO_2 ($\times 10^{-5}$ mol/m^2)	SD ($\times 10^{-5}$ mol/m^2)	Min ($\times 10^{-5}$ mol/m^2)	Max ($\times 10^{-5}$ mol/m^2)
2018	6.4	0.6	5.8	7.9
2019	6.7	0.6	5.8	7.9
2020	6.2	0.6	5.8	7.9
2021	6.8	0.7	5.7	7.8
2022	6.6	0.7	5.6	8.6
2023	7.1	0.7	5.6	9.6
2024	6.8	0.7	5.6	9

The spatial persistence of the hotspot pattern agrees with previous work showing that Kathmandu Valley functions as a bowl-shaped urban basin in which emissions repeatedly accumulate over the same dense urban and traffic-dominated areas (Mahapatra et al., 2019; Panday et al., 2009; Panday & Prinn, 2009). The maps therefore suggest that the pandemic altered the magnitude of NO_2 more than the location of the main pollution burden. This interpretation is also consistent with the topographic setting of Kathmandu valley, where local emissions are superimposed on a strong basin-control signal (Regmi et al. 2003; Mues et al., 2017).

When these levels are placed in global context, Kathmandu is lower in absolute TROPOMI NO_2 burden than many major world cities, but it is not negligible (Table 5). Global and regional studies provide the clearest comparison when their published values are converted to the same unit used in this study.

This comparison shows that annual mean tropospheric NO_2 column in Kathmandu is broadly about half of Los Angeles and Beijing, well below Delhi and Tokyo, and far below Seoul, Dhaka, and Tehran. South Asian TROPOMI analysis also places Dhaka, Delhi, and Lahore above Kolkata in hotspot intensity, with Dhaka showing the strongest NO_2 columns among those four megacities (De Foy & Schauer, 2022). At the same time, direct raw comparison should be treated cautiously. Fioletov et al. (2025) demonstrated that background NO_2 concentrations decline by approximately 50% per kilometer of elevation, and argued that meaningful cross-city comparison requires separation of background and urban emission components where possible. As situated in a high-elevation enclosed basin like Kathmandu, a moderate absolute column density does not preclude significant local air quality stress, as topographic confinement can amplify near-surface pollutant concentrations relative to what column retrievals alone suggest (Chang et al., 2025). Cross city comparisons require careful interpretation because the reported values originate from studies that differ in TROPOMI processing versions, temporal averaging periods, spatial aggregation methods, and statistical treatment of retrievals. Direct equivalence across studies should not be assumed. A common unit conversion was applied to improve visual comparability across cities, while the relative ranking of cities remains consistent after conversion. However, absolute differences across studies are not strictly comparable due to methodological inconsistencies.

Table 5: Comparison of annual mean tropospheric NO_2 column densities for selected cities derived from TROPOMI observations

City	Published metric	Published value	Converted to × 10^{-5} mol m^{-2}	Source
Kathmandu Valley*	Annual mean tropospheric NO_2, 2018–2024	6.2–7.1 × 10^{-5} mol m^{-2}	6.2–7.1	Present study*
Beijing	Median NO_2 TVCD, 2019–2024	144 µmol m^{-2}	14.4	Hassani et al., 2026
Tokyo	Annual mean NO_2 VCD, 2019 and 2024, figure-based approximate values	~10.5 and ~8.5 × 10^{15} molecules cm^{-2}	~17.4 and ~14.1	Huber et al., 2026
Delhi	Annual mean NO_2 VCD, 2019 and 2024, figure-based approximate values	~8.5 and ~7.0 × 10^{15} molecules cm^{-2}	~14.1 and ~11.6	Huber et al., 2026
Los Angeles	Median NO_2 TVCD, 2019–2024	119 µmol m^{-2}	11.9	Hassani et al., 2026
Los Angeles	2024 annual mean NO_2 VCD	7.4 × 10^{15} molecules cm^{-2}	12.3	Huber et al., 2026
Seoul	Annual mean NO_2 VCD, 2019 and 2024, figure-based approximate values	~17.5 and ~12.0 × 10^{15} molecules cm^{-2}	~29.1 and ~19.9	Huber et al., 2026
Dhaka	Median NO_2 TVCD, 2019–2024	216 µmol m^{-2}	21.6	Hassani et al., 2026
Tehran	Median NO_2 TVCD, 2019–2024	294 µmol m^{-2}	29.4	Hassani et al., 2026

3.2 Temporal trends and COVID-19 impact

3.2.1 Medium-term trend analysis:

Medium-term trend analysis using the Theil-Sen estimator revealed a marginally increasing trend of $+5.3 \times 10^{-7}$ mol/m²/year (95% CI: [-1.2×10^{-7}, 1.3×10^{-6}]) across the full study period (Figure 4). However, the Mann-Kendall test indicated no statistically significant trend ($p \geq 0.05$), with the confidence interval spanning zero. The Seasonal Mann-Kendall and pre-whitened Mann-Kendall variants yield consistent results in both magnitude and significance (Table 6).

Sub-period analysis revealed that trends varied across different periods of the study record. No statistically significant trend was detected during the study period. It showed divergent trends as the pre-COVID period (July 2018–February 2020) showed a slight decreasing trend, while the COVID period (March 2020–May 2021) exhibited a stronger decreasing trend, and the recovery period showed an increasing trend. This sequence suggests that the record is dominated more by seasonal structure and short-lived external shocks than by a consistent monotonic trend. However, the relatively short 6.5-year record limits definitive trend detection. Strong seasonal variability (~14% amplitude) and external shocks (COVID-19 lockdown anomaly) may confound the overall trend estimation.

This is supported by known meteorological regime of Kathmandu, where shallow morning mixing, afternoon inflow through mountain gaps, and recurrent recirculation strongly modulate short-term emission shifts through changing ventilation and vertical structure (Regmi et al., 2003; Panday et al., 2009; Panday & Prinn, 2009). The absence of a significant overall trend therefore does not imply a lack of meaningful variability; rather, it indicates that seasonal controls and episodic disruptions were stronger than any gradual directional change across the available record.

Table 6: Seasonal Mann-Kendall and pre-whitened Mann-Kendall trend test results for monthly tropospheric NO_2 column density by season and overall.

Season	Theil-Sen slope (mol m^{-2} yr^{-1})	Classic MK p-value
Winter	1.51E-02	0.834
Pre-monsoon	-3.90E-02	0.289
Monsoon	-1.82E-02	0.646
Post-monsoon	8.18E-02	0.155
Overall (Seasonal MK)	-1.27E-03	0.849
Overall (Pre-whitened MK)	4.67E-04	0.961

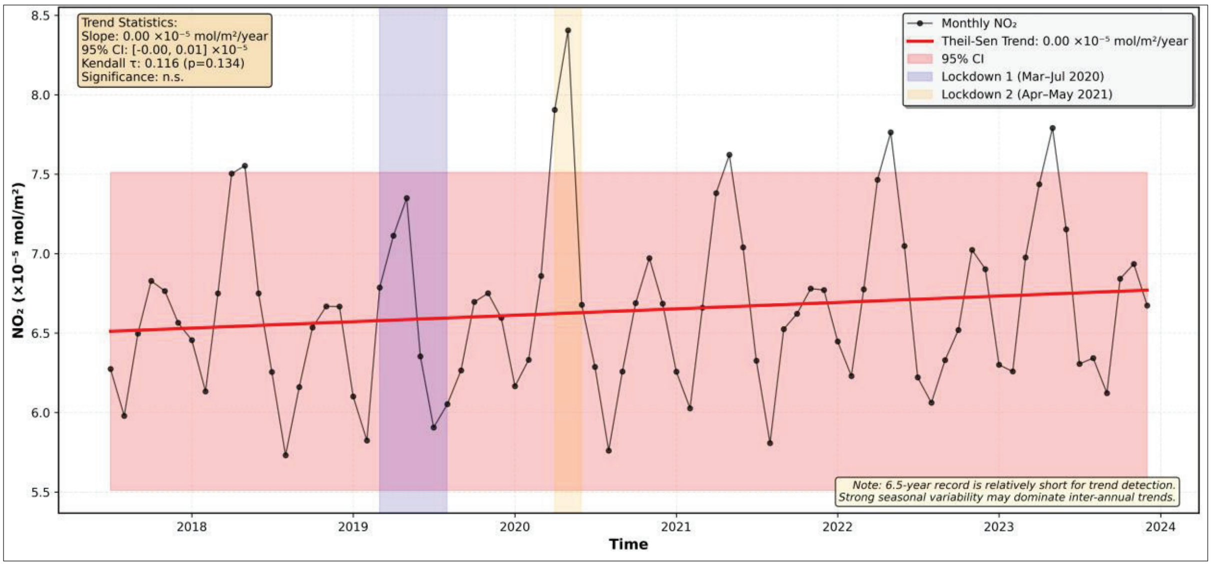

Figure 4: Monthly tropospheric NO_2 time series for Kathmandu Valley (July 2018–December 2024) with Theil-Sen trend line (red) and 95% confidence interval (pink shading). Shaded vertical bands indicate COVID-19 lockdown periods: Lockdown 1 (March–July 2020, blue) and Lockdown 2 (April–May 2021, orange).

3.2.2 COVID-19 impact assessment

The COVID-19 lockdowns had measurable but modest impacts on NO_2 concentrations.

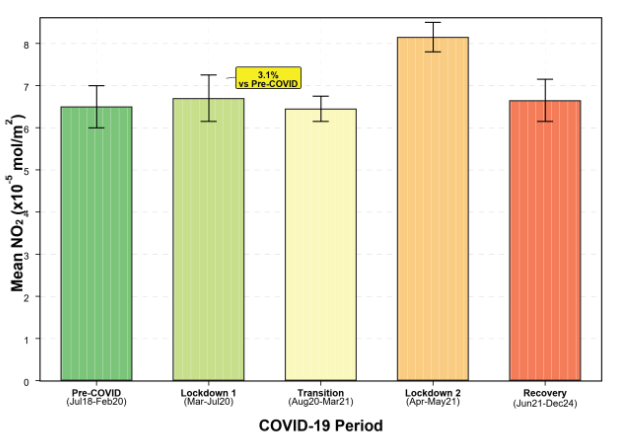

Figure 5: COVID-19 impact assessment on tropospheric NO_2 in Kathmandu Valley. (a) Period comparison of mean NO_2 concentrations across five defined pandemic periods (Pre-COVID, Lockdown 1, Transition, Lockdown 2, Recovery) with error bars showing standard deviation.

Period comparison analysis using the Kruskal-Wallis H-test indicated no statistically significant difference across periods (H = 4.18, $p = 0.38$) (Figure 5; Table 7), consistent with the previous ANOVA result. Pairwise Mann-Whitney U tests with Bonferroni correction confirm no significant differences between any two periods (all $p > 0.5$). Lockdown 1 (March–July 2020) resulted in a 2.7% reduction in mean NO_2 compared to the pre-COVID baseline. The effect size was small (*Cohen's d = 0.31*), indicating modest practical significance.

Same-month comparison analysis: The same-month comparison is the more scientifically defensible estimate of the COVID-19 lockdown signal (Table 8). The same-month comparison confirms modest (~4.5%) reductions during lockdown months, controlling for intra-annual variability, although the 95% bootstrap CI of the overall reduction (–1.4%, +9.9%) spans zero, indicating that the lockdown effect is not statistically significant at $\alpha = 0.05$. This finding is consistent with the temporal trend and annual averages presented in Table 3 because the temporal trend reflects the overall 6.5-year trajectory including pre- and post-lockdown recovery, and annual averages include all months thereby diluting the lockdown signal. The 2020 annual mean (6.2) is lower than other years, consistent with the lockdown effect.

The modest lockdown response is consistent with published evidence for Kathmandu Valley. Dhital et al. (2022) reported a 16.5% NO_2 reduction during the dry-season lockdown segment but only 1.5% during the wet season, and a multi-year monthly composite analysis will recover a smaller net effect than a targeted dry-season comparison. Furthermore, NO_x burden in Kathmandu reflects a mixed source structure that includes brick kilns, industrial combustion, and waste burning

Table 7: NO_2 concentrations by COVID-19 period

Period	Dates	N (months)	Mean NO_2 ($\times 10^{-5}$ mol/m^2)	SD ($\times 10^{-5}$ mol/m^2)
Pre-COVID	Jul 2018–Feb 2020	20	6.6	0.6
Lockdown 1	Mar 2020–Jul 2020	5	6.4	0.1
Transition	Aug 2020–Mar 2021	8	6.4	0.7
Lockdown 2	Apr 2021–May 2021	2	7.4	0.6
Recovery	Jun 2021–Dec 2024	43	6.8	0.7

Table 8: Same month comparison of lockdown and non-lockdown NO2 levels using bootstrap confidence intervals and Wilcoxon test for significance assessment.

Month	Lockdown years Mean ($\times 10^{-5}$ mol m^{-2})	Other Years Mean ($\times 10^{-5}$ mol m^{-2})	Reduction (%)	95% CI of Reduction (%)	p-value (Wilcoxon rank-sum)
March	6.8	7.1	4.2	(-7.7, 15.5)	0.002
April	6.2	6.5	4.6	(-8.3, 16.8)	0.007
May	6.4	6.7	4.5	(-8.0, 16.5)	0
June	6.1	6.3	3.2	(-10.2, 15.8)	0.048
July	6.5	6.7	3	(-9.5, 14.6)	0.003
Overall	6.4	6.66	3.9	(-1.7, 9.3)	0

alongside vehicular traffic (Stockwell et al., 2016; Sadavarte et al., 2019; Zhong et al., 2019), which limits the column-level response to transport-sector restrictions alone.

3.3 Seasonal variability and forest fire sensitivity

NO_2 concentrations exhibited pronounced seasonal cycles, with highest values during the pre-monsoon season (March–May: 7.3 × 10^{-5} mol/m^2) and lowest during the monsoon (June–September: 6.4 × 10^{-5} mol/m^2) and post-monsoon (October–November: 6.4 × 10^{-5} mol/m^2) seasons (Figure 6; Table 9). The pre-monsoon to monsoon ratio of 1.14, indicating a 14% increase shows a clear seasonal amplitude in the valley-wide column burden.

3.3.1 Meteorological context

Monthly boundary-layer height (BLH, ERA5), 10-m wind speed, and precipitation (TRMM/GPM) were correlated with monthly NO_2 anomalies (Table 10). NO_2 anomalies are positively correlated with wind speed (r = +0.20, *p = 0.08*), suggesting that advection of regional pollution contributes to the column burden, and negatively correlated with precipitation (r = –0.14, *p = 0.23*), consistent with wet scavenging during the monsoon. The correlation with BLH is weakly positive (r = +0.10, *p = 0.37*), which is opposite to the expected local-accumulation sign; this is consistent with the column being dominated by regional advection rather than purely local accumulation.

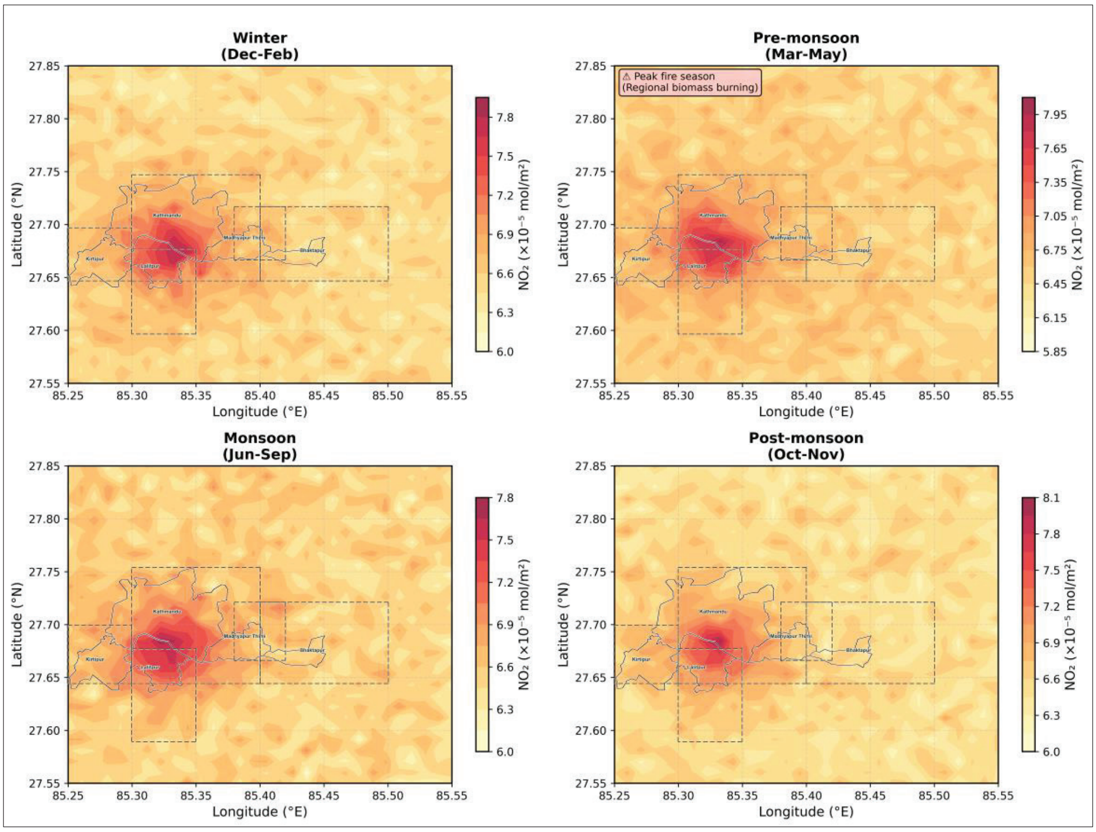

Figure 6: Seasonal mean tropospheric NO_2 spatial distributions across Kathmandu Valley for (a) winter (December–February), (b) pre-monsoon (March–May), (c) monsoon (June–September), and (d) post-monsoon (October–November) during 2018–2024. The pre-monsoon panel notes the coincidence with peak regional forest fire season. Color scales are adjusted per season to show intra-seasonal spatial patterns. The dashed rectangular boxes indicate the analytical zones of the study.

Table 9: Seasonal mean NO_2 concentrations (2018–2024)

Season	Months	Mean NO_2 (× 10^{-5} mol/m^2)	SD (× 10^{-5} mol/m^2)
Winter	Dec–Feb	6.6	1.1
Pre-monsoon	Mar–May	7.3	0.5
Monsoon	Jun–Sep	6.4	0.3
Post-monsoon	Oct–Nov	6.4	0.7

Table 10: Pearson correlation coefficients (r) between monthly tropospheric NO_2 column density anomalies and concurrent meteorological variables from ERA5 reanalysis and TRMM/GPM precipitation

Variable	Pearson r with NO_2	p-value
Boundary-layer height (m)	0.1	0.3732
10-m wind speed (m/s)	0.2	0.084
Precipitation (mm/day)	-0.14	0.2291

3.3.2 Isolation challenges

The elevated NO_2 concentrations observed during the pre-monsoon season reflect the convergence of several emission sources and meteorological conditions. The pre-monsoon period (March–May) coincides with the peak forest fire season across Nepal and the broader Himalayan region. A sensitivity analysis comparing fire season months with non-fire months revealed significantly higher NO_2 during the fire season ($t = 2.34$, $p<0.05$), consistent with a regional biomass burning influence. The observed increase in NO2 during the fire season cannot be attributed solely to wildfire emissions, as seasonal meteorological conditions and local emission sources also influence pollutant concentrations. The significant differences between fire season and non-fire season periods are therefore likely driven by a combination of regional biomass burning, local emissions, and seasonal atmospheric conditions. Separating these individual contributions would require chemical transport modelling, which is beyond the scope of the present study. Regional studies show that the dry pre-monsoon period is associated with stronger pollution transport from the Indo-Gangetic Plain and surrounding source regions into Himalayan valleys (Dhungel et al., 2018). Pre-monsoon enhancement has also been linked to regional open vegetation fires and to entrainment from residual polluted layers (Putero et al., 2015). The present results therefore support the view that fire-season months amplify an already favorable period for NO_2 buildup.

Figure 7 shows the MODIS/VIIRS active fire count time series for the 100-km buffer around Kathmandu Valley, confirming that pre-monsoon fire activity is on average 3.2× higher than during the monsoon. Figure 8 shows 72-hour HYSPLIT back-trajectories, indicating dominant WNW flow during the pre-monsoon that passes over known fire-prone regions of the western Himalaya and Indo-Gangetic Plain. The present results therefore support the view that fire-season months are associated with an already favorable period for NO_2 buildup, but do not allow isolation of the fire contribution from concurrent meteorology and local sources.

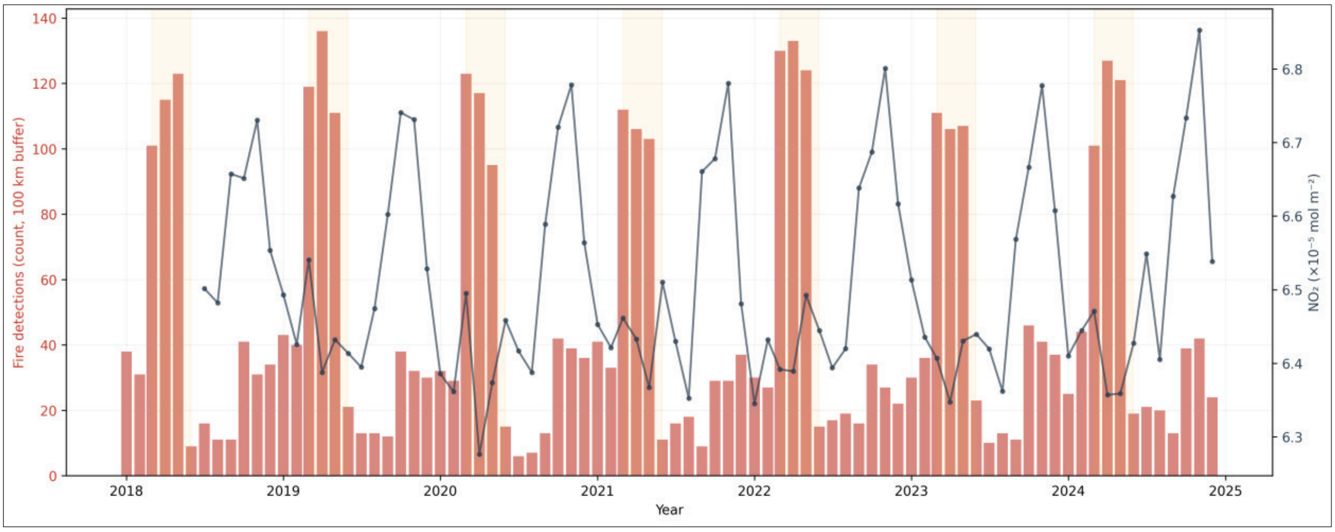

Figure 7: MODIS/VIIRS active fire detections (100 km buffer) and TROPOMI monthly NO_2 in Kathmandu Valley.

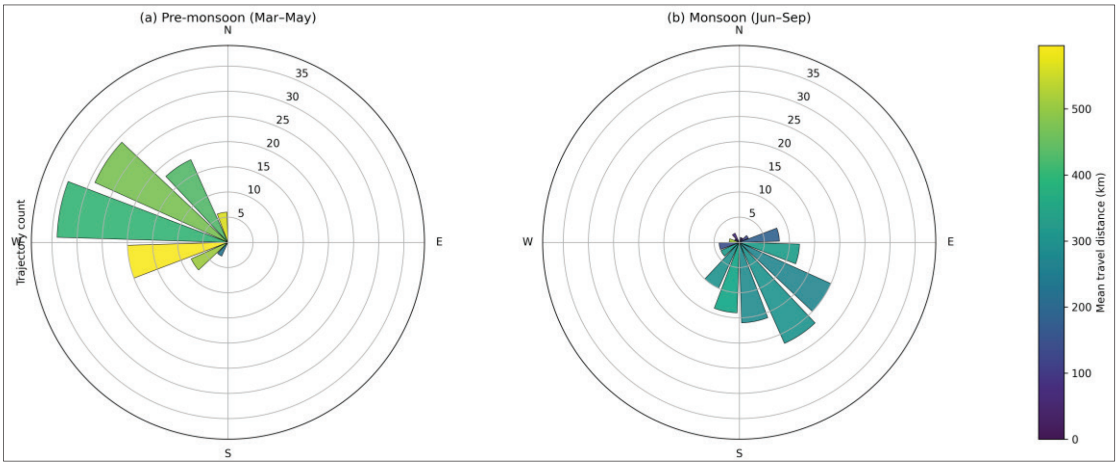

Figure 8: 72-hour HYSPLIT back-trajectories arriving at 500 m AGL over Kathmandu. Pre-monsoon-dominant WNW flow from regional biomass-burning source regions. Monsoon- more dispersed flow with southerly component

Brick kiln operations represent a further plausible source, kilns concentrated in the peri-urban areas of Madhyapur Thimi and Bhaktapur operate at peak capacity during this period to dry and fire bricks before monsoon rains begin (Gyawali et al., 2025). Open burning of agricultural residues following wheat harvest may also contributes to regional NO_x emissions during this window. Meteorology is central to this pattern. Ceilometer observations show that Kathmandu commonly experiences very shallow night and early morning mixing heights of about 150 to 200 m, while daytime development is strongest in pre-monsoon months and much weaker during the monsoon (Mues et al., 2017). Wintertime studies also indicate that weak winds, stable stratification, and low turbulence create strong accumulation. Observational and modeling work further shows that pollutants can be trapped near the surface, lifted into residual layers at night, and re-mixed downward the next morning (Panday & Prinn, 2009; Panday et al., 2009). These processes favor high column burdens in the dry season, particularly when local emissions coincide with regional transport and burning.

Seasonal decomposition analysis identified four anomalous months exceeding ±2σ thresholds, as May 2019 (+0.7 × 10^{-5} mol/m^2), April 2020 (–1.0 × 10^{-5} mol/m^2, COVID lockdown), May 2022 (–0.7 × 10^{-5} mol/m^2), and March 2024 (+0.6 × 10^{-5} mol/m^2). Local seasonal sources likely reinforce the transported signal. NAMaSTE source testing documented emissions from crop residue burning, garbage burning, household combustion, and brick-kiln activity in Nepal (Stockwell et al., 2016). Brick-kiln production is especially relevant in the pre-monsoon period before monsoon rains interrupt operations. Therefore, it can be interpreted that the pre-monsoon maximum reflects the combined effect of unfavorable dispersion, local combustion sources, and regional fire influence rather than a single dominant mechanism.

3.4 Intra-valley spatial variability

Differences between zones reported below are based on rectangular analytical zones defined at the resampled 0.01° grid. Because the native TROPOMI pixel (3.5 × 5.5 km) is comparable to or larger than several of these zones, the differences should be interpreted as broad spatial contrasts rather than fine-scale intra-urban variability. In particular, the boundary between Kathmandu Metropolitan City and Lalitpur Sub-Metropolitan City lies entirely within a single TROPOMI pixel in many places; consequently, the ranking between these two zones should be treated as suggestive rather than definitive.

Significant spatial heterogeneity existed across the five municipalities (Kruskal-Wallis H = 23.4, *$p<0.001$*). Kathmandu zone exhibited the highest mean NO_2 concentration (7.8 × 10^{-5} mol/m^2, CV = 0.15), followed by Madhyapur Thimi (7.6 × 10^{-5} mol/m^2) and Kirtipur (7.5 × 10^{-5} mol/m^2) (Figure 9a; Table 10). Bhaktapur showed the lowest concentrations (7.0 × 10^{-5} mol/m^2, CV = 0.13).

The higher concentrations and greater variability in the urban core of Kathmandu are consistent with high traffic density, dense population, and concentration of built-up areas (Shobnom et al., 2023; Magar, 2025). These spatial contrasts align with prior evidence that urban sites in the valley have substantially higher NO_2 than suburban sites (Kiros et al., 2016). They also fit the broader emissions literature. The Nepal emission inventory identifies diesel vehicles, cement kilns, and brick production as key contributors to NO_x, while also showing that Kathmandu Valley has a disproportionately strong transport and commercial emissions profile relative to its residential contribution (Sadavarte et al., 2019). NAMaSTE-related modeling likewise shows that vehicles and brick kilns are essential for explaining valley air quality and that global inventories severely underestimate important local sources (Zhong et al., 2019). Recent satellite-based analysis further points to cement and brick factories as important contributors to elevated NO_2 in Nepal (Gyawali et al., 2025).

Kathmandu zone concentration was 12% higher than the valley-wide mean (Z-score = +1.8), indicating disproportionate pollution burden. The coefficient of variation (CV) across zones ranged from 0.13 (Bhaktapur, most homogeneous) to 0.15 (Kathmandu, most heterogeneous), reflecting greater spatial variability in the urban core.

This supports the conclusion that the central zone bears the highest NO_2 burden because of concentrated traffic, commercial activity, dense built-up land, and proximity to other combustion sources. The findings suggest that residential cooking contributes less to the observed urban NO_2 distribution in the Kathmandu Valley than vehicular traffic and industrial emissions, although the available evidence does not allow a definitive attribution of source contributions. Satellite columns cannot distinguish sources on their own, and source attribution must rely on inventories and source testing. Household biomass combustion contributes significantly to particulate matter, carbon monoxide,

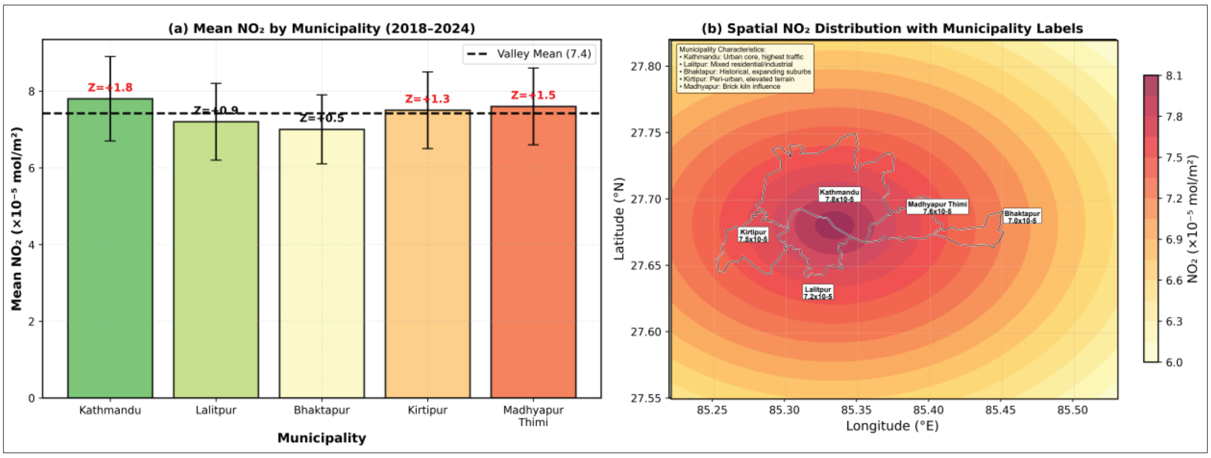

Figure 9: Intra-valley spatial heterogeneity of tropospheric NO_2 (2018–2024). (a) Mean NO_2 concentrations by municipality with error bars showing standard deviation. The dashed line indicates the valley-wide mean (7.4×10^{-5} mol/m^2). Z-scores relative to the valley mean are shown above each bar. (b) Spatial NO_2 distribution with approximate municipal boundaries overlaid and mean concentration labels for each municipality. Color scale shows the full range of mean NO_2 concentrations across the study domain.

Table 11: NO_2 statistics by municipality (2018–2024)

Municipality	Mean NO_2 ($\times 10^{-5}$ mol/m^2)	SD ($\times 10^{-5}$ mol/m^2)	CV	Min ($\times 10^{-5}$ mol/m^2)	Max ($\times 10^{-5}$ mol/m^2)
Kathmandu	7.8	1.1	0.15	5.6	12
Lalitpur	7.2	1	0.13	5.3	11.1
Bhaktapur	7	0.9	0.13	5.2	10.1
Kirtipur	7.5	1	0.13	5.5	11.3
Madhyapur Thimi	7.6	1	0.14	5.5	10.4

and broader combustion pollution in South Asian cities, yet the current evidence does not support treating it as the dominant explanation for the urban NO_2 pattern in Kathmandu Valley (Islam et al., 2020; Stockwell et al., 2016). A more proper interpretation is that NO_2 burden of Kathmandu Valley reflects a mixed combustion system. This study demonstrates that satellite observations provide a scalable and cost-effective alternative for air quality management in developing countries like Nepal.

3.5 Limitations of satellite column interpretation

This study has several limitations related to the use of satellite-derived NO_2 observations. TROPOMI retrievals are subject to uncertainties arising from air mass factor calculations, cloud contamination, and complex terrain effects, which may be particularly important in the mountainous Kathmandu Valley. In addition, the absence of a continuous ground-based NO_2 monitoring network in Nepal limits opportunities for direct validation of satellite observations. Furthermore, satellite NO_2 columns represent vertically integrated concentrations and cannot independently distinguish between local emissions, transported pollution, or specific emission sources.

The reported trends were not meteorologically normalized and may therefore reflect both emission changes and atmospheric variability. The use of approximate analysis zones rather than official administrative boundaries may also introduce minor spatial classification errors. Finally, satellite NO_2 columns do not directly represent ground-level exposure, especially in mountain basins where boundary layer dynamics and pollutant transport can strongly influence the vertical distribution of NO_2. Therefore, the results are most useful for identifying spatial patterns, seasonal variability, and long-term trends, while ground-based measurements remain essential for exposure assessment and source verification.

4. Conclusion

This study presents a medium -term spatiotemporal assessment of tropospheric NO_2 in Kathmandu Valley using Sentinel-5P TROPOMI satellite observations. Valley-wide concentrations remained statistically stable over the study period, with no statistically significant trend detected during the study period. COVID-19 lockdowns produced modest emission reductions, indicating that residential and industrial sources persisted while transport declined. Pronounced seasonal cycles peaked during pre-monsoon, coincident with regional biomass burning, forest fire, brick kiln operations, and unfavorable meteorology. The available evidence supports these as plausible contributing factors but does not by itself allow quantitative attribution to any single driver. Significant spatial heterogeneity placed the highest pollution burden in Kathmandu zone, with peripheral areas showing lower concentrations. Overall, the results support the use of satellite observations as a robust tool for tracking spatiotemporal NO_2 patterns in data-sparse mountain cities like Kathmandu.

Based on the findings, stratified spatially adaptive emission control strategies on the basis of pollutant concentration and integration of high-resolution satellite data into national emission inventory as a complementary tool are recommended. Satellite column densities can be integrated with ground-based measurements for health-relevant assessments as a complementary tool to provide a more complete picture of NO_2 exposure in the valley.

References

Aryal, R. K., Lee, B.-K., Karki, R., Gurung, A., Baral, B., & Byeon, S.-H. (2009). Dynamics of PM2.5 concentrations in Kathmandu Valley, Nepal. *Journal of Hazardous Materials*, *168*(2–3), 732–738. https://doi.org/10.1016/j.jhazmat.2009.02.086

Bhatta, B. P., Kadel, M., Pandey, G. N., Adhikari, S., & Bhat, M. K. (2024). Spatiotemporal analysis of air pollutants before, during and after COVID-19 outbreak over Kathmandu Valley. *Journal of Land Management and Geomatics Education*, *6*, 8–17.

CBS. (2021). *National Population and Housing Census 2021*.

Cleveland, R. B., Cleveland, W. S., McRae, J. E., & Terpenning, I. (1990). STL: A seasonal-trend decomposition procedure based on LOESS. *Journal of Official Statistics*, *6*(1), 3–73.

Cohen, J. (1988). *Statistical power analysis for the behavioral sciences* (2nd ed.). Lawrence Erlbaum Associates.

Collaud Coen, M., Andrews, E., Bigi, A., Martucci, G., Romanens, G., Vogt, F. P. A., & Vuilleumier, L. (2020). Effects of the prewhitening method, the time granularity, and the time segmentation on the Mann–Kendall trend detection and the associated Sen's slope. *Atmospheric Measurement Techniques*, *13*(12), 6945–6964. https://doi.org/10.5194/amt-13-6945-2020

Davtalab, M., Byθenkienλ, S., & Bimbaitλ, V. (2023). Long-term spatial and temporal evaluation of the PM2.5 and PM10 mass concentrations in Lithuania. *Atmospheric Pollution Research*, *14*(12), 101951. https://doi.org/10.1016/j.apr.2023.101951

Dhital, N. B., Bhattarai, D. R., Sapkota, R. P., Rijal, K., Byanju, R. M., & Yang, H.-H. (2022). Comparing the Change in Air Quality during the COVID-19 Lockdown between Dry and Wet Seasons in Nepal. *Aerosol and Air Quality Research*, *22*(8), 220201. https://doi.org/10.4209/aaqr.220201

Dhungel, S., Kathayat, B., Mahata, K., & Panday, A. (2018). Transport of regional pollutants through a remote trans-Himalayan valley in Nepal. *Atmospheric Chemistry and Physics*, *18*(2), 1203–1216. https://doi.org/10.5194/acp-18-1203-2018

Giri, J., Raut, S., Rimal, B., Adhikari, R., Joshi, T. P., & Shah, G. (2023). Impact of air pollution on human health in different geographical locations of Nepal. *Environmental Research*, *226*, 115669. https://doi.org/10.1016/j.envres.2023.115669

Gocic, M., & Trajkovic, S. (2013). Analysis of changes in meteorological variables using Mann-Kendall and Sen's slope estimator statistical tests in Serbia. *Global and Planetary Change*, *100*, 172–182. https://doi.org/10.1016/j.gloplacha.2012.10.014

Gorelick, N., Hancher, M., Dixon, M., Ilyushchenko, S., Thau, D., & Moore, R. (2017). Google Earth Engine: Planetary-scale geospatial analysis for everyone. *Remote Sensing of Environment*, *202*, 18–27. https://doi.org/10.1016/j.rse.2017.06.031

Gurung, A., & Bell, M. L. (2013). The state of scientific evidence on air pollution and human health in Nepal. *Environmental Research*, *124*, 54–64. https://doi.org/10.1016/j.envres.2013.03.007

Gurung, A., Levy, J. I., & Bell, M. L. (2017). Modeling the intraurban variation in nitrogen dioxide in urban areas in Kathmandu Valley, Nepal. *Environmental Research*, 155, 42–48. https://doi.org/10.1016/j.envres.2017.01.038

Gyawali, M. S., Lamsal, L. N., Neupane, S., Gyawali, B., Bhattarai, K., Fisher, B., Krotkov, N., Van Geffen, J., Eskes, H., Sharma, S., Brunt, C., & Aryal, R. (2025). Cement and brick factories contribute elevated levels of NO2 pollution in Nepal: Evidence of high-resolution view from space. *Atmospheric Environment: X*, 26, 100324. https://doi.org/10.1016/j.aeaoa.2025.100324

Hassan, F., Chaudhry, M. U., Yasir, M., Asghar, M. N., & Sarkodie, S. A. (2021). Monitoring the Impact of COVID-19 Lockdown on the Production of Nitrogen Dioxide (NO2) Pollutants Using Satellite Imagery: A Case Study of South Asia. *Sustainability*, *13*(13), 7184. https://doi.org/10.3390/su13137184

Hassani, A., Walker, S.E., Stebel, K., & Schneider, P. (2026). Tracking the path to cleaner cities using global NO_2 monitoring from space. *Environ.Res. Lett.*, 094004. https://doi/org/10.1088/1748-9326/ae5e97.

Health Effects Institute. (2023). *South asia – a regional air quality snapshot*. State of Global Air. https://www.stateofglobalair.org/sites/default/files/documents/2023-09/soga_reg._aq_snapshot_9-11-23_final.pdf

Hedelt, P., Efremenko, D.S., Loyola, D.G., Spurr, R., & Clarisse, L. (2019). Sulfur dioxide layer height retrieval from Sentinel-5 Precursor/TROPOMI using FP_ILM. *Atmos. Meas.Tech.,* 12,5503-5517. https://doi.org/10.5194/amt-12-5503-2019

Hirsch, R. M., Slack, J. R., & Smith, R. A. (1982). Techniques of trend analysis for monthly water quality data. *Water Resources Research*, *18*(1), 107–121. https://doi.org/10.1029/WR018i001p00107

Hoyer, S., & Hamman, J. (2017). xarray: N-D labeled Arrays and Datasets in Python. *Journal of Open Research Software*, *5*(1), 10. https://doi.org/10.5334/jors.148

Huber, D.E., Kerr, G.H., Nawaz, M.O., Runkel, S., Anenberg, S.C., & Goldberg, D.L. (2026). Global NO2 changes between 2019 and 2024 as observed by TROPOMI in urban areas and emerging hotspots. *Atmos.Chem.Phys., 26, 3783-3803.* https://doi.org/10.5194/acp-26-3783-2026

Hunter, J. D. (2007). Matplotlib: A 2D Graphics Environment. *Computing in Science & Engineering*, *9*(3), 90–95. https://doi.org/10.1109/MCSE.2007.55

Ishtiaque, A., Shrestha, M., & Chhetri, N. (2017). Rapid Urban Growth in the Kathmandu Valley, Nepal: Monitoring Land Use Land Cover Dynamics of a Himalayan City with Landsat Imageries. *Environments*, *4*(4), 72. https://doi.org/10.3390/environments4040072

Islam, Md. R., Jayarathne, T., Simpson, I. J., Werden, B., Maben, J., Gilbert, A., Praveen, P. S., Adhikari, S., Panday, A. K., Rupakheti, M., Blake, D. R., Yokelson, R. J., DeCarlo, P. F., Keene, W. C., & Stone, E. A. (2020). Ambient air quality in the Kathmandu Valley, Nepal, during the pre-monsoon: Concentrations and sources of particulate matter and trace gases. *Atmospheric Chemistry and Physics*, *20*(5), 2927–2951. https://doi.org/10.5194/acp-20-2927-2020

Jarvis, D. J., Adamkiewicz, G., & Héroux, M. E. (2010). Nitrogen dioxide. In *WHO guidelines for indoor air quality: Selected pollutants*. World Health Organization. https://www.ncbi.nlm.nih.gov/books/NBK138707/

Kendall, M. G. (1975). *Rank correlation methods* (4th ed.). Charles Griffin.

Kiros, F., Shakya, K. M., Rupakheti, M., Regmi, R. P., Maharjan, R., Byanju, R. M., Naja, M., Mahata, K., Kathayat, B., & Peltier, R. E. (2016). Variability of Anthropogenic Gases: Nitrogen Oxides, Sulfur Dioxide, Ozone and Ammonia in Kathmandu Valley, Nepal. *Aerosol and Air Quality Research*, *16*(12), 3088–3101. https://doi.org/10.4209/aaqr.2015.07.0445

Kitada, T., & Regmi, R. P. (2003). Dynamics of air pollution transport in late wintertime over kathmandu valley, nepal: As revealed with numerical simulation. *Journal of Applied Meteorology*, *42*(12), 1770–1798. https://doi.org/10.1175/1520-0450(2003)042%3C1770:doapti%3E2.0.co;2

Kruskal, W. H., & Wallis, W. A. (1952). Use of ranks in one-criterion variance analysis. *Journal of the American Statistical Association*, *47*(260), 583–621. https://doi.org/10.1080/01621459.1952.10483441

Kuikel, S., Pokharel, B., & Bhattarai, N. (2024). The effect of wildfires on air quality in Kathmandu, Nepal. *Environmental Advances*, *15*, 100493. https://doi.org/10.1016/j.envadv.2024.100493

Latif, M., Syed, F. S., & Hannachi, A. (2017). Rainfall trends in the South Asian summer monsoon and its related large-scale dynamics with focus over Pakistan. *Climate Dynamics*, *48*, 11–12, 3565–3581. https://doi.org/10.1007/s00382-016-3284-3

Magar, K. (2025). Inspecting gaseous pollutants and their dynamics in Kathmandu using satellite derived data. *GeoFocus Revista Internacional de Ciencia y Tecnología de La Información Geográfica*, *36*, 43–62. https://doi.org/10.21138/GF.835

Mahapatra, P. S., Puppala, S. P., Adhikary, B., Shrestha, K. L., Dawadi, D. P., Paudel, S. P., & Panday, A. K. (2019). Air quality trends of the Kathmandu Valley: A satellite, observation and modeling perspective. *Atmospheric Environment*, *201*, 334–347. https://doi.org/10.1016/j.atmosenv.2018.12.043

Mann, H. B. (1945). Nonparametric Tests Against Trend. *Econometrica*, *13*(3), 245. https://doi.org/10.2307/1907187

Mishra, M., & Kulshrestha, U. C. (2021). A Brief Review on Changes in Air Pollution Scenario over South Asia during COVID-19 Lockdown. *Aerosol and Air Quality Research*, *21*(4), 200541. https://doi.org/10.4209/aaqr.200541

Moore, G. W. K., & Semple, J. L. (2021). Himalaya Air Quality Impacts From the COVID 19 Lockdown Across the Indo Gangetic Plain. *GeoHealth*, *5*(6), e2020GH000351. https://doi.org/10.1029/2020GH000351

Mues, A., Rupakheti, M., Münkel, C., Lauer, A., Bozem, H., Hoor, P., Butler, T., & Lawrence, M. G. (2017). Investigation of the mixing layer height derived from ceilometer measurements in the Kathmandu Valley and implications for local air quality. *Atmospheric Chemistry and Physics*, *17*(13), 8157–8176. https://doi.org/10.5194/acp-17-8157-2017

Öçer, N. E., Matcý, D. K., & Avdan, U. (2024). Monitoring the impact of the Corona pandemic on nitrogen dioxide emissions at large scales via Google Earth Engine. *Acta Geographica Slovenica*, *64*(3). https://doi.org/10.3986/AGS.13454

Panday, A. K., & Prinn, R. G. (2009). Diurnal cycle of air pollution in the Kathmandu Valley, Nepal: Observations. *Journal of Geophysical Research: Atmospheres*, *114*(D9), 2008JD009777. https://doi.org/10.1029/2008JD009777

Panday, A. K., Prinn, R. G., & Schär, C. (2009). Diurnal cycle of air pollution in the Kathmandu Valley, Nepal: 2. Modeling results. *Journal of Geophysical Research: Atmospheres*, *114*(D21), 2008JD009808. https://doi.org/10.1029/2008JD009808

Prunet, P., Lezeaux, O., Camy-Peyret, C., & Thevenon, H. (2020). Analysis of the NO_2 tropospheric product from S5P TROPOMI for monitoring pollution at city scale. *City and Environment Interactions*, *8*, 100051. https://doi.org/10.1016/j.cacint.2020.100051

Putero, D., Cristofanelli, P., Marinoni, A., Adhikary, B., Duchi, R., Shrestha, S. D., Verza, G. P., Landi, T. C., Calzolari, F., Busetto, M., Agrillo, G., Biancofiore, F., Di Carlo, P., Panday, A. K., Rupakheti, M., & Bonasoni, P. (2015). Seasonal variation of ozone and black carbon observed at Paknajol, an urban site in the Kathmandu Valley, Nepal. *Atmospheric Chemistry and Physics*, *15*(24), 13957–13971. https://doi.org/10.5194/acp-15-13957-2015

Regmi, R. P., Kitada, T., & Kurata, G. (2003). Numerical Simulation of Late Wintertime Local Flows in Kathmandu Valley, Nepal: Implication for Air Pollution Transport. *Journal of Applied Meteorology*, *42*(3), 389–403. https://doi.org/10.1175/1520-0450(2003)042%3C0389:NSOLWL%3E2.0.CO;2

Sadavarte, P., Rupakheti, M., Bhave, P., Shakya, K., & Lawrence, M. (2019). Nepal emission inventory – Part I: Technologies and combustion sources (NEEMI-Tech) for 2001–2016. *Atmospheric Chemistry and Physics*, *19*(20), 12953–12973. https://doi.org/10.5194/acp-19-12953-2019

Seabold, S., & Perktold, J. (2010). *Statsmodels: Econometric and Statistical Modeling with Python*. 92–96. https://doi.org/10.25080/Majora-92bf1922-011

Sen, P. K. (1968). Estimates of the Regression Coefficient Based on Kendall's Tau. *Journal of the American Statistical Association*, *63*(324), 1379–1389.

Sharma, B. R., Kuttippurath, J., Gopikrishnan, G. S., & Pathak, M. (2023). Trends in atmospheric pollution in the Third Pole: Analyses of tropospheric NO_2 for the period 2005–2020. *Environmental Science: Atmospheres*, *3*(5), 905–918. https://doi.org/10.1039/D2EA00075J

Shobnom, N., Hossain, S., & Roni, R. (2023). Monitoring spatiotemporal changes of NO2 using TROPOMI and sentinel-5 images for Dhaka city and its surrounding areas of Bangladesh. *Journal of Air Pollution and Health*. https://doi.org/10.18502/japh.v8i3.13785

Shrestha, S. R., Kim Oanh, N. T., Xu, Q., Rupakheti, M., & Lawrence, M. G. (2013). Analysis of the vehicle fleet in the Kathmandu Valley for estimation of environment and climate co-benefits of technology intrusions. *Atmospheric Environment*, *81*, 579–590. https://doi.org/10.1016/j.atmosenv.2013.09.050

Stockwell, C. E., Christian, T. J., Goetz, J. D., Jayarathne, T., Bhave, P. V., Praveen, P. S., Adhikari, S., Maharjan, R., DeCarlo, P. F., Stone, E. A., Saikawa, E., Blake, D. R., Simpson, I.

J., Yokelson, R. J., & Panday, A. K. (2016). Nepal Ambient Monitoring and Source Testing Experiment (NAMaSTE): Emissionsof trace gases and light-absorbing carbon from wood and dung cooking fires,garbage and crop residue burning, brick kilns, and other sources. *Atmospheric Chemistry and Physics*, *16*(17), 11043–11081. https://doi.org/10.5194/acp-16-11043-2016

Tack, F., Merlaud, A., Iordache, M.-D., Danckaert, T., Yu, H., Fayt, C., Meuleman, K., Deutsch, F., Fierens, F., & Van Roozendael, M. (2017). High-resolution mapping of the NO_2 spatial distribution over Belgian urban areas based on airborne APEX remote sensing. *Atmospheric Measurement Techniques*, *10*(5), 1665–1688. https://doi.org/10.5194/amt-10-1665-2017

Theil, H. (1950). A rank-invariant method of linear and polynomial regression analysis, part I; confidence regions for the parameters of polynomial regression equations. *Proceedings of the Royal Netherlands Academy of Sciences*, *53*, 386–392.

Upadhyay, A., Mahapatra, P. S., Singh, P. K., Dahal, S., Pokhrel, S., Bhujel, A., Joshi, I. B., Paudel, S. P., Puppal, S. P., & Adhikary, B. (2022). Learnings from COVID-19 Forced Lockdown on Regional Air Quality and Mitigation Potential for South Asia. *Aerosol and Air Quality Research*, *22*(4), 210376. https://doi.org/10.4209/aaqr.210376

Van Geffen, J., Eskes, H., Compernolle, S., Pinardi, G., Verhoelst, T., Lambert, J.-C., Sneep, M., Ter Linden, M., Ludewig, A., Boersma, K. F., & Veefkind, J. P. (2022). Sentinel-5P TROPOMI NO_2 retrieval: Impact of version v2.2 improvements and comparisons with OMI and ground-based data. *Atmospheric Measurement Techniques*, *15*(7), 2037–2060. https://doi.org/10.5194/amt-15-2037-2022

Veefkind, J. P., Aben, I., McMullan, K., Förster, H., De Vries, J., Otter, G., Claas, J., Eskes, H. J., De Haan, J. F., Kleipool, Q., Van Weele, M., Hasekamp, O., Hoogeveen, R., Landgraf, J., Snel, R., Tol, P., Ingmann, P., Voors, R., Kruizinga, B., … Levelt, P. F. (2012). TROPOMI on the ESA Sentinel-5 Precursor: A GMES mission for global observations of the atmospheric composition for climate, air quality and ozone layer applications. *Remote Sensing of Environment*, *120*, 70–83. https://doi.org/10.1016/j.rse.2011.09.027

Vîrghileanu, M., Săvulescu, I., Mihai, B.-A., Nistor, C., & Dobre, R. (2020). Nitrogen Dioxide (NO2) Pollution Monitoring with Sentinel-5P Satellite Imagery over Europe during the Coronavirus Pandemic Outbreak. *Remote Sensing*, *12*(21), 3575. https://doi.org/10.3390/rs12213575

Virtanen, P., Gommers, R., Oliphant, T. E., Haberland, M., Reddy, T., Cournapeau, D., Burovski, E., Peterson, P., Weckesser, W., Bright, J., Van Der Walt, S. J., Brett, M., Wilson, J., Millman, K. J., Mayorov, N., Nelson, A. R. J., Jones, E., Kern, R., Larson, E., … Vázquez-Baeza, Y. (2020). SciPy 1.0: Fundamental algorithms for scientific computing in Python. *Nature Methods*, *17*(3), 261–272. https://doi.org/10.1038/s41592-019-0686-2

Zhang, X., & Zwiers, F.W. (2004). Comment on "Applicability of prewhitening to eliminate the influence of serial correlation on the Mann-Kendall test" by Sheng Yue and Chun Yuan Wang. *Water Resources Research*, 40. https://doi.org/10.1029/2003WR002073.

Zhang, R., Zhang, Y., Lin, H., Feng, X., Fu, T.-M., & Wang, Y. (2020). NOx Emission Reduction and Recovery during COVID-19 in East China. *Atmosphere*, *11*(4), 433. https://doi.org/10.3390/atmos11040433

Zhong, M., Saikawa, E., Avramov, A., Chen, C., Sun, B., Ye, W., Keene, W. C., Yokelson, R. J., Jayarathne, T., Stone, E. A., Rupakheti, M., & Panday, A. K. (2019). Nepal Ambient Monitoring and Source Testing Experiment (NAMaSTE): Emissions of particulate matter and sulfur dioxide from vehicles and brick kilns and their impacts on air quality in the Kathmandu Valley, Nepal. *Atmospheric Chemistry and Physics*, *19(12), 8209–8228. https://doi.org/10.5194/acp-19-8209-2019*